A model to estimate carbon dioxide injectivity and storage capacity for geological sequestration in shale gas wells

Supporting Information

Ryan W. J. Edwards,[*,†] Michael A. Celia,[†] Karl W. Bandilla,[†] Florian Doster,[‡] Cynthia M. Kanno[†,∞]

[†]Department of Civil and Environmental Engineering, Princeton University, Princeton, NJ 08544, United States

[‡]Institute of Petroleum Engineering, Heriot-Watt University, Edinburgh EH14 4AS, United Kingdom

[∞]Current Address: Civil and Environmental Engineering, Colorado School of Mines, 1500 Illinois St, Golden, CO 80401, United States

*Corresponding Author. Phone: 347-906-0484. E-mail: rwje@princeton.edu

Table of Contents

S1. Model Initial and Boundary Conditions 2

S2. Adsorption Model Derivation 3

S3. Numerical Solution 4

S4. Data Selection and Filtering Procedure 6

- **Data Source** 6
- **Data Filtering Procedure** 6
- **Region Delineation** 6
- **Well Lateral Length Estimation** 7

S5. Parameter Matching Procedure 7

S6. Injection Simulation Parameters 8

S7. Constant-Rate Injection Pressure Plot 9

S8. Constant-Pressure Injection Adsorption Contribution Plots 10

References 12

S1. Model Initial and Boundary Conditions

Mathematically, the initial conditions for all scenarios are:

$$p(x,0) = p_I \qquad \omega_c(x,0) = \omega_{c_I} = 0 \tag{S.1}$$

where p_I is the initial pressure and ω_{c_I} is the initial mass fraction of CO_2 (zero). Different initial pressure is selected for natural gas production or CO_2 injection scenarios.

In all scenarios the boundary condition at the plane of symmetry ($x = d$) is a no flow boundary for both the pressure and transport equations:

$$\left.\frac{dp}{dx}\right|_{x=d} = 0 \qquad \left.\frac{d\omega_c}{dx}\right|_{x=d} = 0 \tag{S.2}$$

There are two different boundary conditions at the fracture face ($x = 0$) boundary depending on the model scenario. For the constant-pressure CO_2 injection (and for natural gas production scenarios for history-matching) there is a fixed pressure and fixed composition:

$$p(0,t) = p_f \tag{S.3}$$

$$\omega_c(0,t) = \omega_{c_f} \tag{S.4}$$

where p_f is the pressure in the hydraulic fractures (bottom well pressure) and ω_{c_f} is the CO_2 mass fraction at the fracture face (1 for CO_2 injection, 0 for natural gas production). For injection, p_f is higher than p_I, and vice-versa for production.

For the constant-rate CO_2 injection scenario there is a fixed total CO_2 mass flux (advective plus diffusive flux) at the boundary:

$$\begin{aligned} q_{c_f}(0,t) &= -\frac{\omega_{c_f}\rho^b\left(\omega_{c_f}, p_f\right)\kappa}{\mu^b\left(\omega_{c_f}, p_f\right)}\left.\frac{dp}{dx}\right|_{x=0} - \phi S_g \rho^b\left(\omega_{c_f}, p_f\right) D_c \left.\frac{d\omega_c}{dx}\right|_{x=0} \\ &= \omega_{c_f}\rho^b\left(\omega_{c_f}, p_f\right) u_f^b - \phi S_g \rho^b\left(\omega_{c_f}, p_f\right) D_c \left.\frac{d\omega_c}{dx}\right|_{x=0} \end{aligned} \tag{S.5}$$

where u_f^b is the advective volumetric bulk flux at the boundary and q_{c_f} is the total CO_2 mass flux (total CO_2 mass flow rate per unit area of hydraulic fracture), which can be calculated from the total CO_2 mass injection rate into the horizontal well, $\not{t}_c$:

$$q_{c_f} = \frac{\not{t}_c}{2n_f a_f} = \frac{\not{t}_c}{2n_f HV} \tag{S.6}$$

where n_f is the number of hydraulic fractures, a_f is the surface area of each fracture plane, and H and V are the horizontal width and vertical height of each hydraulic fracture plane.

The boundary condition for the CO_2 component equation in the constant-rate scenario is the fixed composition (Eq. S.4) and fixed CO_2 mass flux (Eq. S.6). The boundary condition for the pressure equation is fixed composition and fixed bulk volumetric flux:

$$u_f^b(0,t) = \frac{q_{c_f}}{\omega_{c_f}\rho^b\left(\omega_{c_f}, p_f\right)} + \frac{\phi S_g D_c \left.\frac{d\omega_c}{dx}\right|_{x=0}}{\omega_{c_f}} \tag{S.7}$$

Eq. S.7 prescribes the bulk volumetric (advective) flux, u_f^b, such that the total CO_2 mass flux, q_{c_f}, remains constant at the prescribed rate. u_f^b varies with time during an injection simulation since the composition gradient at the boundary, $\left.\frac{d\omega_c}{dx}\right|_{x=0}$ (and therefore the diffusive flux) varies.

S2. Adsorption Model Derivation

A model for two-component excess adsorption is derived beginning with the definition of excess adsorption, Eq. 8:

$$n^e = n^t - V_a\rho^b \tag{S.8}$$

where n^e is the excess amount adsorbed and n^t is the total (absolute) amount adsorbed. The adsorbed phase volume can be expressed in terms of the total amount adsorbed and the adsorbed phase density, ρ_a:

$$V_a = \frac{n^t}{\rho_a} \tag{S.9}$$

Eq. S.9 is substituted into Eq. S.8:

$$n^e = n^t - \frac{n^t}{\rho_a}\rho^b \tag{S.10}$$

$$n^e = n^t\left(1 - \frac{\rho^b}{\rho_a}\right) \tag{S.11}$$

ρ_a is assumed to be constant, while ρ^b is a function of the gas composition and pressure. The multicomponent Langmuir equation (Eq. 7) is now substituted for n^t, and adsorbed amount is expressed as a bulk adsorbed mass density (mass adsorbed per unit rock volume):

$$\rho_1^e = \rho_1^{max}\frac{K_1 p_1}{1 + K_1 p_1 + K_2 p_2}\left(1 - \frac{\rho_1^b(\omega_1, p)}{\rho_{a,1}(\omega_1, p)}\right) \tag{S.12}$$

where ρ_1^e is the excess adsorbed mass density of component 1, ρ_1^b is the bulk gas density of component 1, which can be expressed as $\omega_1\rho^b$, and $\rho_{a,1}$ is the adsorbed phase density of component 1, which can be expressed as $\omega_1^a\rho_a$. Substituting these expressions into Eq. S.12 gives the final modified two-component Langmuir model used to estimate excess adsorption:

$$\rho_1^e = \rho_1^{max} \frac{K_1 p_1}{1 + K_1 p_1 + K_2 p_2} \left(1 - \frac{\omega_1 \rho^b(\omega_1, p)}{\omega_1^a(\omega_1, p)\rho_a}\right) \tag{S.13}$$

The equation can be applied for each of the two components in the system.

S3. Numerical Solution

The modified Picard iteration finite difference approximation for the pressure equation (Eq. 2) is:

$$\begin{aligned} C_{i,p}^{n+1,m} \frac{\delta_i^{P,m}}{\Delta t} \Delta x + C_{i,\omega}^{n+1,m} \frac{\delta_i^{W,m}}{\Delta t} \Delta x - D_i^{n+1,m} \frac{\delta_{i+1}^{P,m} - \delta_i^{P,m}}{\Delta x} + D_{i-1}^{n+1,m} \frac{\delta_i^{P,m} - \delta_{i-1}^{P,m}}{\Delta x} \\ = -\frac{\left(\phi S_g \rho_i^b + \rho_{c,i}^a + \rho_{m,i}^a\right)^{n+1,m} - \left(\phi S_g \rho_i^b + \rho_{c,i}^a + \rho_{m,i}^a\right)^n}{\Delta t} \Delta x \\ + D_i^{n+1,m} \frac{P_{i+1}^{n+1,m} - P_i^{n+1,m}}{\Delta x} - D_{i-1}^{n+1,m} \frac{P_i^{n+1,m} - P_{i-1}^{n+1,m}}{\Delta x} \end{aligned} \tag{S.14}$$

where n denotes the n^{th} timestep, m is the iteration number, and the solution is known at time n as well as time $n+1$ and iteration m but unknown at time $n+1$ and iteration $m+1$, and the primary variables evaluated at the 'new' timestep $(n+1)$ and new iteration level $(m+1)$ are the unknowns to be determined in the modified Picard iterative algorithm. The variable $\Delta t = t^{n+1} - t^n$ is the timestep size, Δx is the (uniform) cell size, i denotes the cell number from 1 to N, $P_i^{n+1,m}$ is the approximate value of p in cell i at time $n+1$ and iteration level m, $W_i^{n+1,m}$ is the approximate value of ω in cell i at time $n+1$ and iteration level m, $\delta_i^{P,m}$ is the difference $P_i^{n+1,m+1} - P_i^{n+1,m}$, $\delta_i^{W,m}$ is the difference $W_i^{n+1,m+1} - W_i^{n+1,m}$, $C_{i,p}^{n+1,m}$ is the partial derivative of the mass densities (see Eq. 2) with respect to p evaluated using the solution at the previous iteration $n+1, m$, $C_{i,\omega}^{n+1,m}$ is similarly the partial derivative of the mass densities with respect to ω, and $D_i^{n+1,m}$ is the Darcy mass flux coefficient (see Eq. 2). $C_i^{n+1,m}$ and $D_i^{n+1,m}$ are non-linear functions of p and ω.

The approximation for the transport equation (Eq. 3) is:

$$\begin{aligned} A_{i,\omega}^{n+1,m} \frac{\delta_i^{W,m}}{\Delta t} \Delta x + A_{i,p}^{n+1,m} \frac{\delta_i^{P,m}}{\Delta t} \Delta x + u_{i+\frac{1}{2}}^{b,n+1,m} \rho_i^{b,n+1,m} \delta_i^{W,m} \\ - u_{i-\frac{1}{2}}^{b,n+1,m} \rho_{i-1}^{b,n+1,m} \delta_{i-1}^{W,m} - B_i^{n+1,m} \frac{\delta_{i+1}^{W,m} - \delta_i^{W,m}}{\Delta x} \\ + B_{i-1}^{n+1,m} \frac{\delta_i^{W,m} - \delta_{i-1}^{W,m}}{\Delta x} \\ = -\frac{\left(\phi S_g \rho_i^b W_i + \rho_{c,i}^a\right)^{n+1,m} - \left(\phi S_g \rho_i^b W_i + \rho_{c,i}^a\right)^n}{\Delta t} \Delta x \\ - u_{i+\frac{1}{2}}^{b,n+1,m} \rho_i^{b,n+1,m} W_i^{n+1,m} + u_{i-\frac{1}{2}}^{b,n+1,m} \rho_{i-1}^{b,n+1,m} W_{i-1}^{n+1,m} \\ + B_i^{n+1,m} \frac{P_{i+1}^{n+1,m} - P_i^{n+1,m}}{\Delta x} - B_{i-1}^{n+1,m} \frac{P_i^{n+1,m} - P_{i-1}^{n+1,m}}{\Delta x} \end{aligned} \tag{S.15}$$

where $A_{i,\omega}^{n+1,m}$ is the partial derivative of the CO_2 mass densities (see Eq. 3) with respect to ω, $A_{i,p}^{n+1,m}$ is the partial derivative of the CO_2 mass densities with respect to p, $B_i^{n+1,m}$ is the diffusive mass flux coefficient (see Eq. 3), and $u_{i\pm\frac{1}{2}}^{b,n+1,m}$ is the Darcy bulk gas flux evaluated at the cell boundary (see Eq. 4). $A_i^{n+1,m}$ and $B_i^{n+1,m}$ are nonlinear functions of p and ω.

A key reason to write the finite difference equations in this form is that the right hand side terms are exactly the mass balance that we wish to satisfy (that is, we wish to force those terms to be exactly zero) for each time step. The sum over all grid cells of the right side terms is a measure of the error of the solution at the m^{th} iteration (the amount by which the solution fails to satisfy the finite difference approximation mass balance), defined as the residual. For convergence of the iteration, both the residual error and the iteration differentials $\delta_i^{P,m}$ and $\delta_i^{W,m}$ approach zero. Since the right hand side is the mass balance, this solution form guarantees mass conservation. This scheme was required as mass balance errors of ~30% were observed at early times when using simple non-iterative methods due to the nonlinearity of the coefficients and the large changes in pressure and composition at early times in the simulations. The equations were solved simultaneously, also due to issues caused by the nonlinearities if the equations were solved sequentially. The numerical solution was implemented in MATLAB.

Once the equations have been solved for a particular set of conditions to yield a set of pressures and gas compositions for all cells and time steps in the simulation, the flux of CO_2 into the shale reservoir matrix from the hydraulic fracture can be calculated for the cases where fixed pressure is assigned to the fracture boundary. This is achieved by multiplying the total CO_2 flux at the fracture boundary of the domain by the hydraulic fracture surface area and number of hydraulic fractures to determine the flux for the entire horizontal well:

$$\begin{aligned} \not{f}_c^n &= -2n_f a_f \rho^b(\omega_{c_f}, p_f)\left[\omega_{c_f}\frac{\kappa}{\mu^b(\omega_{c_f}, p_f)}\frac{dp}{dx}\bigg|_{x=0}^{n} + \phi S_g D_c \frac{d\omega_c}{dx}\bigg|_{x=0}\right] \\ &= -2n_f HV\rho^b(\omega_{c_f}, p_f)\left[\omega_{c_f}\frac{2\kappa}{\mu^b(\omega_{c_f}, p_f)}\left(\frac{P_1^n - p_f}{\Delta x}\right)\right. \\ &\left. + 2\phi S_g D_c\left(\frac{W_1^n - \omega_f}{\Delta x}\right)\right] \end{aligned} \tag{S.16}$$

where $\not{f}_c^n$ is the mass flux of CO_2 into the entire horizontal well at time n, a_f is the surface area of each fracture plane, H and V are the horizontal width and vertical height of each hydraulic fracture plane, P_1^n is the solution for pressure in the first cell (adjacent to the fracture boundary) at time n, and W_1^n is similarly the solution for CO_2 mass fraction. n_f is the number of hydraulic fractures, calculated by:

$$n_f = \frac{L}{2d} \tag{S.17}$$

where L is the total lateral length of the horizontal well and d is half the distance between adjacent hydraulic fractures (assumes constant fracture spacing).

The cumulative mass flux is calculated by multiplying the flux for each time step by Δt and summing over all time steps. The cumulative boundary mass flux is also necessarily equal to the

sum of mass accumulation in all cells in the domain as a condition of the imposition of numerical mass balance.

S4. Data Selection and Filtering Procedure

Data Source

Shale gas well production data were obtained from Drilling Info, Inc.[1] For the Barnett Shale, wells commencing production in 2007 – 2011 inclusive (10,197 wells) were selected. This period was chosen as it represents the peak period of well drilling in the Barnett Shale. For the Marcellus Shale, wells in Pennsylvania commencing production in 2010 - June 2014 (4,778 wells) were selected. This period was chosen because the number of producing wells in the Marcellus was relatively small beforehand and began increasing significantly from 2010.

Data Filtering Procedure

The raw data were filtered to remove unsuitable wells from the analysis. The procedure for the Barnett Shale data was as follows:

1. Remove vertical wells.
2. Remove all plugged and abandoned wells with cumulative production <0.25 Bcf.
3. Remove inactive wells with cumulative production <0.25 Bcf.
4. Remove wells missing all cumulative gas production and production rate decline data.
5. Remove oil and water wells.
6. Remove production data from average calculations with any evidence of shutting in wells or re-fracturing (3-month decline > 12-month decline, 12-month > 24-month, or 24-month > 60-month).

1,228 out of 10,179 wells (12%) were removed from the raw data set.

The procedure for the Marcellus Shale data differed from the Barnett due to differences in data format and availability between Pennsylvania and Texas. The procedure for Marcellus Shale data was as follows:

1. Remove vertical wells.
2. Estimate lateral length (see well lateral length estimation description).
3. Remove suspicious total depth and estimated lateral length data (total depth <5000ft or estimated lateral length <500m) *note production data not removed, only depth data.
4. Remove all shut-in wells with cumulative production <0.25 Bcf.
5. Remove inactive wells with cumulative production <0.25 Bcf.
6. Remove wells with zero cumulative gas production.
7. Remove wells with 6-month cumulative production <500Mcf (evidence that they were shut in or managed).

533 out of 4,778 wells (11%) were removed from the raw data set.

Region Delineation

The Marcellus Shale in Pennsylvania was divided into two regions for data analysis and model history-matching: northeast and southwest PA. The region delineation is shown in Figure S.1.

Wells in Allegheny, Armstrong, Beaver, Butler, Fayette, Greene, Indiana, Washington and Westmoreland counties were classified as southwest (1,449 wells). Wells in Bradford, Lycoming, Sullivan, Susquehanna, Tioga, Wyoming counties were classified as northeast (2,516 wells). 280 out of the 4,245 filtered Marcellus wells were not in these counties and therefore not used in the history-matching analysis.

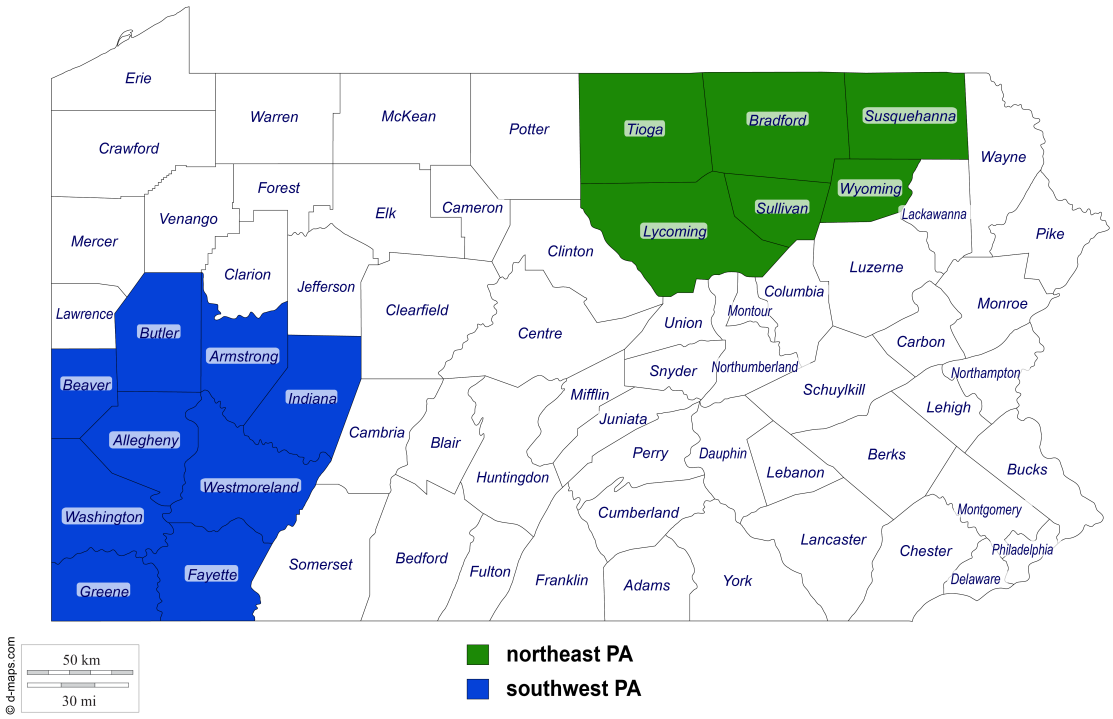

Figure S.1. County map of Pennsylvania showing delineation of southwest and northeast PA regions. The map is a modified version of a free map obtained from d-maps.com.[2]

Well Lateral Length Estimation

The horizontal well lateral length was estimated by a different method for each play:

In well data from Texas, the production interval (PI) of the wells is reported. In a typical horizontal well the PI is essentially the horizontal lateral length, so it was assumed that lateral length was equal to PI length.

For Pennsylvania, PI is not available in the well data. Lateral length was estimated by subtracting the estimated depth of the Marcellus shale at each well's location (by GIS analysis) from the reported total depths (the total length of the vertical and horizontal portions of a well).

S5. Parameter Matching Procedure

Production data were averaged for wells commencing production within different subset periods for each play. Data for several time points in well production history were used, including 6, 12 and 24 months since commencement of production and later time points depending on the age of the well. For each subset of wells, the production data from the individual wells were averaged. For Barnett wells the subset period for data averaging was yearly increments; for Marcellus wells it was generally 6-monthly increments. The averaged production data for each subset were used

for parameter history-matching. There were differences in data availability and consequently matching method for the Barnett and Marcellus: for Barnett wells, both cumulative gas production and production rate data were used to match wells, but for the Marcellus only cumulative gas production was used since production data were reported on 6-monthly (rather than monthly) increments. Six-month averaged rates are not able to capture rate-decline behavior in sufficient detail. The averaged production data for each subset were plotted. The shale reservoir model (in single-component mode using natural gas fluid properties) was then adjusted to visually fit the averaged production data by adjusting the model parameters. Parameter matches were made for each region and for three different parameter scenarios:

- A 'best-fit average well' scenario that used the average lateral length of all wells in the total data sample and matched model production curves to average production data of subset periods that had similar well length. Best estimate adsorption parameters were used.
- A 'low' scenario that also used the average well length and matched to average production data of subset periods with similar well length, but instead changed the parameter combination to one that would fit the production data at early time but result in lower ultimate production beyond the history-matching period (i.e. higher permeability but lower porosity, adsorption and pressure – see Table S.2).
- A 'high' scenario that used the average well length for the most recent subset period with at least 12 months production history and matched to these data (which have higher production than the overall average due to longer well lateral length). The scenario represented by this match is one where the length of new wells continues increasing into the future such that the average for all wells in a region reaches that of the recent wells. Adsorption parameters at the high end of the estimated uncertainty range were also selected (see Table S.2), which result in higher ultimate production.

S6. Injection Simulation Parameters

The reservoir and well parameters history-matched to natural gas production data and used for the CO_2 injection simulations are shown in Tables S.1-S.3. Additional parameters required for the CO_2 injection simulations that were not matched in the single-component history-matching are also included (gas dispersion coefficient and CO_2 sorption parameters). Two parameter groups govern the production or injection behavior of the model: the interference time and total gas in place. The interference times associated with each scenario are shown in Table S.3. References in the tables indicate information sources that guided parameter selections.

Table S.1 – Reservoir parameters for both plays that are consistent in all parameter scenarios.

Shale Play	**Gas Saturation (%)** [3-6]	**CH_4 Langmuir K (MPa^{-1})** [7]	**CO_2 Langmuir K (MPa^{-1})** [8]	**Reservoir Temperature (°C)** [3]	**Gas Dispersion Coefficient (m^2/s)** [9,10]	**Fracture Face Pressure (production) / Initial Pressure (injection) (MPa)** [11]	**Adsorbed Phase Density, ρ_a (kg/m^3)** [12]
Marcellus	75	0.17	0.1	60	1×10^{-9}	3.5	1000
Barnett	75	0.17	0.1	80	1×10^{-9}	3.5	1000

Table S.2 – Reservoir parameters for each region and each history-matching parameter scenario. Shaded boxes show parameters that were varied in the history-match to fit the model to the observations, while unshaded boxes show parameters selected based on well data or literature.

Shale Play & Scenario	Porosity (%) [3,5,13,14]	Reservoir Pressure (production) / Max. Pressure (injection) (MPa) [3,5,6,15]	Effective Permeability (nanoDarcy)	Max. CH_4 Adsorption (kg/m^3) [7,8]	Max. CO_2 Adsorption (kg/m^3) [8,16,17]
Marcellus SW Avg.	6	35	25	6.5	55
High	6	35	25	8.5	70
Low	5	33	30	4.5	40
Marcellus NE Avg.	6	35	20	6.5	55
High	6	35	20	8.5	70
Low	5	33	25	4.5	40
Barnett Avg.	6	25	45	5	45
High	6	25	45	7	60
Low	5	24	45	3	30

Table S.3 – Well parameters for each region and each history-matching parameter scenario. Shaded boxes show parameters that were varied in the history-match to fit the model to the observations, while unshaded boxes show parameters selected based on well data or literature. The interference time is calculated by Eq. 11 using the selected parameters for each scenario.

Shale Play & Scenario	Lateral Length (m)	Fracture Height, V (m)	Fracture Width, H (m) [11]	Fracture Spacing, 2d (m) [4,18]	Interference Time, τ (years)
Marcellus SW Avg.	1556	32	200	30	6.6
High	1644	32	200	24	4.2
Low	1556	32	200	30	5.0
Marcellus NE Avg.	1675	50	200	30	6.8
High	1759	50	200	28	5.9
Low	1675	50	200	30	5.0
Barnett Avg.	872	30	200	30	5.8
High	1000	30	200	30	5.8
Low	872	30	200	30	5.0

S7. Constant-Rate Injection Pressure Plot

For the constant-rate injection scenario, pressure at the fracture face (bottom well injection pressure) increases with time until it reaches the allowable maximum pressure and the injection is ceased. Figure S.2 shows examples of the pressure increase with time for several selected injection rates in the northeast PA Marcellus Shale. Figure 6 in the main text relates to this graph

by showing the time taken to reach the maximum allowable pressure for all injection rates between 5 to 120 tonnes per day.

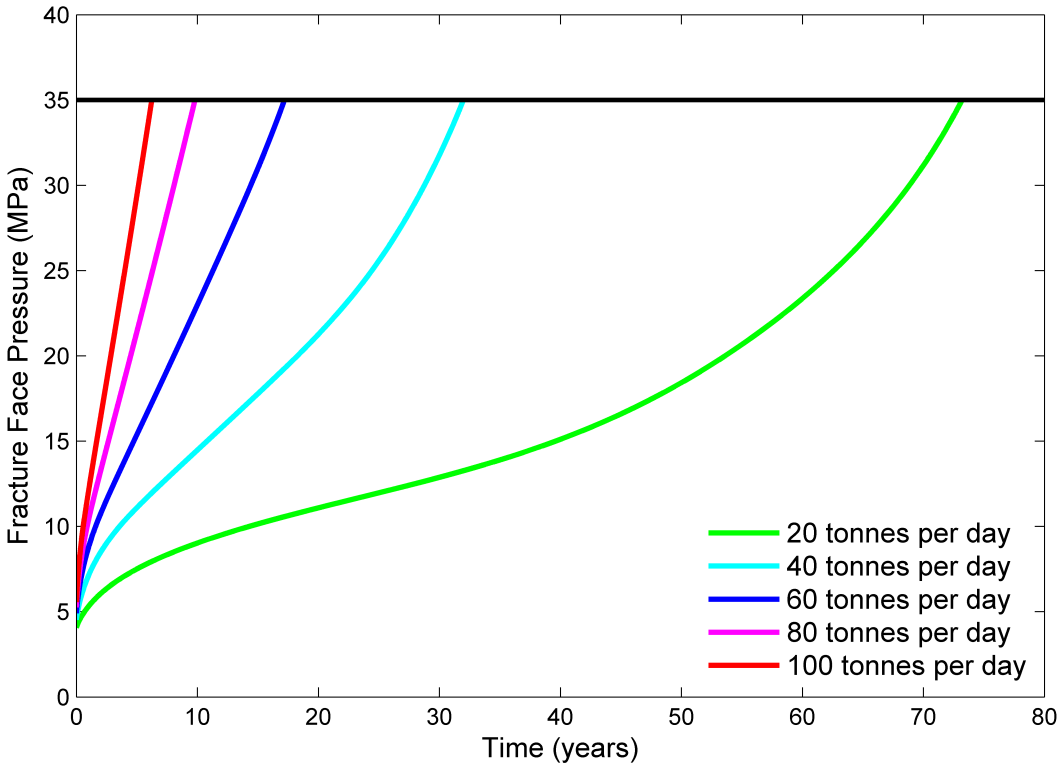

Figure S.2. Marcellus Shale northeast PA fracture face (injection) pressure versus time for five different constant injection rates and maximum allowable pressure 35 MPa.

S8. Constant-Pressure Injection Adsorption Contribution Plots

The cumulative total CO_2 injected in the constant-pressure injection simulations, shown in Figure 7 in the main text, is composed of CO_2 in the pore space and adsorbed CO_2. The Marcellus Shale northeast PA and Barnett Shale best estimate cumulative plots are re-produced in Figure S.3, with the contributions of excess and absolute adsorbed CO_2 to the total mass stored also shown. Excess adsorption is used in the model, and the model pressure and composition solution was used to calculate the implied absolute adsorption using Eq. 7. Figure S.3 shows that while excess adsorption is relatively small (approximately 15% of the total CO_2 in the shale after 40 years of injection in the Marcellus, and 30% in the Barnett), the absolute amount of adsorbed CO_2 is actually a large fraction of the total mass stored. Absolute adsorption constitutes the majority of CO_2 stored within the shale for both the Marcellus (90%) and Barnett (75%). Excess adsorption is relatively small because the density of supercritical CO_2 at high pressure in the shale approaches the density of the adsorbed phase, resulting in only a small density difference between the adsorbed and supercritical CO_2 phases.

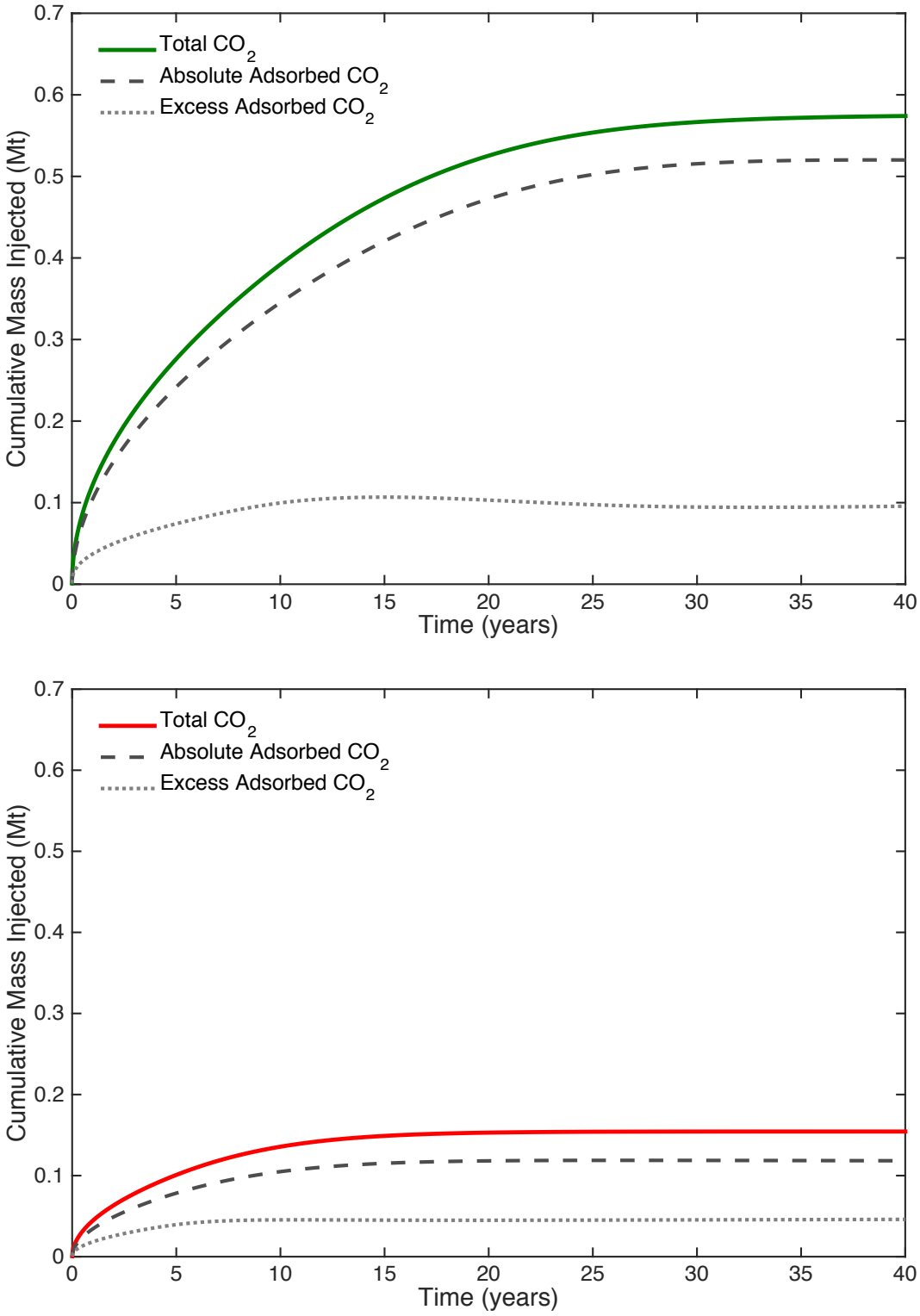

Figure S.3. Simulated cumulative total mass of CO_2 injected with time for constant-pressure injection in an average well in the Marcellus Shale in northeast PA (top), and Barnett Shale (bottom), with the absolute adsorbed (dashed) and excess adsorbed (dotted) masses of CO_2 shown. The cumulative total is the sum of the pore space and adsorbed CO_2.

References

1. *Drillinginfo, Inc.* Website; info.drillinginfo.com.
2. d-maps.com: Pennsylvania; http://d-maps.com/carte.php?&num_car=21437&lang=en.
3. NETL *A Comparative Study of the Mississippian Barnett Shale, Fort Worth Basin, and Devonian Marcellus Shale, Appalachian Basin*; DOE/NETL-2011/1478; National Energy Technology Laboratory, US Department of Energy: 2011.
4. Byrnes, A. P., Role of Induced and Natural Imbibition in Frac Fluid Transport and Fate in Gas Shales. In *US EPA Technical Workshop for the Hydraulic Fracturing Study: Fate and Transport*, EPA: Arlington, VA, 2011.
5. Bowker, K. A., Barnett Shale gas production, Fort Worth Basin: Issues and discussion. *AAPG Bull.* **2007,** *91*, (4), 523-533.
6. Engelder, T., Capillary tension and imbibition sequester frack fluid in Marcellus gas shale. *Proc. Natl. Acad. Sci. U. S. A.* **2012,** *109*, (52), E3625-E3625.
7. Zhang, T. W.; Ellis, G. S.; Ruppel, S. C.; Milliken, K.; Yang, R. S., Effect of organic-matter type and thermal maturity on methane adsorption in shale-gas systems. *Org. Geochem.* **2012,** *47*, 120-131.
8. Nuttall, B. C.; Eble, C. F.; Drahovzal, J. A.; Bustin, R. M. *Analysis of Devonian Black Shales in Kentucky for Potential Carbon Dioxide Sequestration and Enhanced Natural Gas Production*; DE-FC26-02NT41442; Kentucky Geological Survey: Lexington, KY, 2005.
9. Finley, R. J., An overview of the Illinois Basin - Decatur Project. *Greenhouse Gases-Science and Technology* **2014,** *4*, (5), 571-579.
10. Liu, F. Y.; Ellett, K.; Xiao, Y.; Rupp, J. A., Assessing the feasibility of CO2 storage in the New Albany Shale (Devonian-Mississippian) with potential enhanced gas recovery using reservoir simulation. *Int. J. Greenh. Gas Control* **2013,** *17*, 111-126.
11. Patzek, T. W.; Male, F.; Marder, M., Gas production in the Barnett Shale obeys a simple scaling theory. *Proc. Natl. Acad. Sci. U. S. A.* **2013,** *110*, (49), 19731-19736.
12. Weniger, P.; Kalkreuth, W.; Busch, A.; Krooss, B. M., High-pressure methane and carbon dioxide sorption on coal and shale samples from the Parana Basin, Brazil. *Int. J. Coal Geol.* **2010,** *84*, (3-4), 190-205.
13. Chalmers, G. R.; Bustin, R. M.; Power, I. M., Characterization of gas shale pore systems by porosimetry, pycnometry, surface area, and field emission scanning electron microscopy/transmission electron microscopy image analyses: Examples from the Barnett, Woodford, Haynesville, Marcellus, and Doig units. *AAPG Bull.* **2012,** *96*, (6), 1099-1119.
14. Vega, B.; Dutta, A.; Kovscek, A. R., CT Imaging of Low-Permeability, Dual-Porosity Systems Using High X-ray Contrast Gas. *Transport in Porous Media* **2013**, 1-17.
15. Jarvie, D. M.; Hill, R. J.; Ruble, T. E.; Pollastro, R. M., Unconventional shale-gas systems: The Mississippian Barnett Shale of north-central Texas as one model for thermogenic shale-gas assessment. *AAPG Bull.* **2007,** *91*, (4), 475-499.
16. Godec, M.; Koperna, G.; Petrusak, R.; Oudinot, A., Potential for enhanced gas recovery and CO2 storage in the Marcellus Shale in the Eastern United States. *Int. J. Coal Geol.* **2013,** *118*, 95-104.
17. NYSERDA *Geologic, Engineering and Economic Evaluation of the CO2 Sequestration Capacity of New York's Gas Shales*; 12-02; New York State Energy Research and Development Authority: 2011; p 76.

18. Thompson, J. W.; Fan, L.; Grant, D.; Martin, R. B.; Kanneganti, K. T.; Lindsay, G. J., An Overview of Horizontal-Well Completions in the Haynesville Shale. *J. Can. Pet. Technol.* **2011,** *50*, (6), 22-35.